



Signal Detection and Enhancement for Seismic Crosscorrelation Using the Wavelet-Domain Kalman Filter

Yang Zhao¹ · Fenglin Niu² · Zhishuai Zhang³ · Xiang Li⁴ · Jinhong Chen⁵ · Jidong Yang⁶

Received: 23 March 2020 / Accepted: 3 October 2020
© Springer Nature B.V. 2020

Abstract

Crosscorrelation is a classical signal-processing technique that plays an important role in exploration and earthquake geophysics. Seismic velocity estimation utilizes the crosscorrelation between observed and predicted seismic records in traveltime tomography. The crosscorrelation between two stations represents the Green's functions retrieved from ambient noises in passive seismic interferometry. It can be used to estimate the subsurface velocity and amplitude information. The calculation of crosscorrelation usually assumes that the input data are stationary; however, the real seismic data are often non-stationary, due to the presence of multiple wave-modes and background noises. The seismic crosscorrelations often have low signal-to-noise ratio and frequently fail to provide correct information for subsequent processing. To address this problem, we develop a comprehensive technique to reduce contamination and improve the quality of crosscorrelation in the wavelet domain. The new procedure includes the forward wavelet transformation of raw records, the crosscorrelation between wavelet coefficients, single-channel image object detection, multi-channel Kalman-filter object tracking, and inverse wavelet transformation to produce the new crosscorrelation gathers. We effectively remove the unwanted components associated with contaminated wave-modes as the proposed detection and tracking algorithm can accurately extract the target wave-mode. We validate the method for three datasets: a marine streamer survey, a borehole survey, and a broadband dataset from seismology stations. We demonstrate that the proposed method can significantly improve the signal-to-noise ratio of the seismic crosscorrelations, considerably enhancing the quality of the data for subsequent advanced crosscorrelation-based seismic processing.

Keywords Crosscorrelation · Kalman filtering · Wave-mode separations · Object tracking

✉ Yang Zhao
zhaoyang@cup.edu.cn

Extended author information available on the last page of the article

1 Introduction

Crosscorrelation is a powerful signal-processing tool and extensively adopted in pattern recognition and signal detection among different industries, such as acoustics, medical applications, and geophysics. It projects one signal onto another as a means of measuring how much of the second signal is present in the first, so it can detect the presence of known signals as components of more complicated signals (Keane and Adrian 1992). Crosscorrelation of pressure transients and acoustic waves was applied for leak detection and location in the pipeline network of water authorities (Hafezi and Mirhosseini 2015). An active radar with omnidirectional sensors used crosscorrelation to measure the travel time difference between a forward signal, that was transmitted, and a received backscattered signal, to estimate the range of a radar target (Silvia 1987). In clinical ultrasounds, the crosscorrelation function between the transmissions and reflections recorded with ultrasound transducers coupled to the skin could measure the geometry of different tissues (Viola and Walker 2003).

The usage of crosscorrelated seismic waveforms plays an essential role in several stages in geophysics (Yilmaz 2001). For instance, in travelttime-based velocity building methods, the crosscorrelation between observed and calculated records (Luo and Schuster 1991) extracted phase shifts to constrain subsurface velocity models. When the compared waveforms were simple and similar, the travelttime difference between two traces was estimated by selecting the lag that corresponds to the peak of the crosscorrelation (Knapp and Carter 1976; Sun et al. 2016). Crosscorrelation methods usually assume that the input data are stationary, whereas this is not the case for most of the applications due to the presence of multi-wave modes. This argument is no longer valid in cases with inequivalent amplitude spectra associated with complex multi-wave modes (Van Der Hilst and De Hoop 2005). Another important geophysical application is seismic interferometry: a stack of crosscorrelations of traces recorded by two receivers over sources that were uniformly distributed in three-dimensional (3D) heterogeneous earth could retrieve the Green's function activated at one receiver and received by the other (Curtis et al. 2009). This assertion applied to passive-source records in the ambient noise ranges from borehole microseismic (Grechka and Zhao 2012) to global seismology (Niu et al. 2008). The reconstructed Green's function retrieved from crosscorrelations of ambient noises produced either P- or S-waves traveling between the receivers, which were then transferred to subsurface velocities at different scales. However, the assumptions of an enclosing boundary of sources behind seismic interferometry were often not satisfied in most acquisitions (Zhao and Li 2018a). It, therefore, produced a low signal-to-noise ratio (SNR) crosscorrelation gathers and unreliable Green's functions. Interferometric data required advanced processing to restore the coverage in a way that crosscorrelation can still work effectively (Nakata et al. 2011).

Similar to crosscorrelation, the wavelet transform was widely used in acoustics, medical applications, and geophysics areas (Mallat and Zhang 1993). It decomposes a signal into a series of time-scale wavelet coefficients. The scale measures, which are closely related to frequency, can be used to analyze and filter data (Diallo et al. 2006; Yu et al. 2007). Crosscorrelation was also computed in the wavelet domain (Li and Nozaki 1997) and was extensively applied in Earth science studies of river runoffs and global climatic index analysis (Labat 2005). In addition to this time series analysis, Kalman filtering can function as a powerful spatial algorithm for recursively updating a prediction of a system by processing a succession of measurements over distances. After each spatial measurement, a new offset prediction is produced by the filter's measurement step (Bishop and Welch 2001).

It uses a series of measurements containing statistical noise and other inaccuracies, so the algorithm can produce estimates of unknown variables that tend to be more accurate than those based on a single measurement alone. Kalman filters demonstrated its usefulness in various applications such as navigation satellite systems and computer graphics because of its relatively simple form and require small computational power. Although some excellent geophysics works in the literature employed the Kalman filter for seismic deconvolution (Crump 1974) and time-lapse seismic history matching (Emerick and Reynolds 2012), the industry has not fully taken advantage of these power algorithms, for example, by performing them into the multi-dimensional spatial, frequency, and time domain. Specifically, the travelttime estimation in velocity estimation and passive seismic interferometry with large-offset acquisitions contains informative correlated wave-modes in all dimensions. The quality of the extracted signal depends on the extent to which crosscorrelated wave-modes are interrelated at different frequencies, and how these time–frequency quantities move along spatial locations.

Microseismic event detection and denoising have been in rapid growth in the application of hydraulic fracturing in the past 20 years, and its nature is very close to the purpose of this study. Mousavi et al. (2016) utilized synchrosqueeze continuous wavelet transform and custom thresholding to remove strong background noises and detect small-amplitude microseismic events. Chen (2018) decomposed a microseismic trace into an ensemble of components using non-stationary least-square inversion and filtered out the random noises via least-square fitting of multiple damping exponential components. Based on mathematical morphology, Li et al. (2016) introduced a non-stationary weighting operator into the process of decomposing the data to several morphological multiscale components and reconstructed these morphological components to remove microseismic noises. Machine learning became one of the most popular microseismic processing techniques in recent years. Chen (2017) developed an unsupervised machine learning to help cluster the time samples into microseismic waveforms and non-waveforms. Three clustering features (mean, power, short-, and long-time-average trigger) are selected and able to detect microseismic arrivals successfully in very noisy environments. Alternatively, Qu et al. (2019) used support vector machine classification with a Gaussian kernel achieve fast and accurate detections of microseismic events. Zhang et al. (2020) combined the continuous wavelet transform and the convolutional neural network for waveform classification and arrival pickings. Saad and Chen (2020) later expanded it with convolutional autoencoder to extract the scalogram and then feed them into the K-means clustering algorithm to distinguish microseismic waveform and non-waveform components.

Although many geophysical applications can be adapted to this proposed workflow, the scope of this paper is limited to crosscorrelation-based travelttime-difference estimation and passive seismic interferometry (Zhao et al. 2019, 2020). We develop a new method using crosscorrelation in the wavelet domain that exploits non-stationary variations to simplify the complexity of correlation gathers associated with noise contaminations via a Kalman filter. Specifically, the method maps data from the time—offset (TX) domain into the time—frequency (TF) domain. The multi-mode non-stationary gathers are then decomposed into several simple, single-mode, and stationary components. The Kalman filter robustly detects and tracks the target wave-mode via a sequence of spatial locations from these correlated constituents. The new method consists of the following steps: (1) transforming seismic records to the wavelet domain before applying crosscorrelation; (2) crosscorrelating the wavelet coefficients; (3) detecting target wave-modes via image segmentation in the TF domain; (4) tracking target wave-modes via Kalman filtering in the time–frequency–offset (TFX) domain; (5) transforming the filtered wavelet coefficients

back to the TX domain. This method allows effective measurements of target wave-modes, using image segmentation and Kalman filtering for the wavelet-domain correlation coefficients. Meanwhile, it effectively attenuates non-desired wave-modes and produces much higher SNR crosscorrelation functions, leading to high-quality data for subsequent seismic velocity estimation at different scales.

2 Crosscorrelation

Crosscorrelation is a measure of similarity for two seismic traces as a function of the time delay of one trace relative to the other, known as a sliding inner product. Mathematically, the crosscorrelation function M between two seismic traces is written as

$$M(\tau) = \int_0^T X_A(t)X_B(t + \tau)dt, \tag{1}$$

where X_A and X_B represent the observed and calculated data, respectively. The misfit function χ is expressed as an optimization problem when the relative phase shift τ between the observed and calculated data is zero. It seeks a τ (less than the absolute value of record time T) that shifts a calculated trace so that it matches the observed trace. Since seismic data are stochastic processes, it is implied that definitions involve ensemble averages rather than time integration. The criterion for the best match is defined as the travel time difference $\Delta\tau$ that maximizes the crosscorrelation function M , i.e.,

$$\chi(\tau_{\max}) = \max\{M(\tau)|\tau \in [-T, T]\}. \tag{2}$$

Note that $\Delta\tau = 0$ indicates that the correct velocity model has been found, which generates the wave arriving at the same time as the observed data. In the context of seismic interferometry, X_A and X_B denote passive seismic datasets recorded at the spatial coordinates of the two receivers, respectively. M is the resulting interferometric data with the correlation time-lag length τ at the receiver B when A is treated as a virtual source. $\chi(\tau_{\max})$ provides an indirect measurement of apparent velocity along with the receiver array.

In real applications, X_A and X_B usually contain multi-wave modes:

$$\begin{aligned} X_A(t) &= X_A^{tar}(t) + X_A^n(t) + \dots \\ X_B(t + \tau) &= X_B^{tar}(t + \tau) + X_B^n(t + \tau) + \dots \end{aligned} \tag{3}$$

where superscripts *tar* and *n* are the target wave-modes and unwanted noisy wavefields recorded at the receiver A and B , respectively. Only the crosscorrelation between $X_A^{tar}(t)$ and $X_B^{tar}(t)$ would form a correct kinematic event, whereas other terms typically generate spurious events. Usually, the target wave-modes are the transmission waves in travelttime tomography, or the body P-wave propagating around the borehole in downhole passive interferometry or the fundamental mode Rayleigh waves in ambient noise interferometry. The noises are the unwanted wave-modes superimposed with target wave-modes recorded at receivers.

Figures 1 and 2 illustrate simple and complicated crosscorrelation examples, respectively. The conventional crosscorrelation method is capable of providing a correct time-delay for the two single wave-mode (i.e., target wave-mode) traces in Fig. 1. Because of the multi-wave-mode traces (Fig. 2), the conventional crosscorrelation produces ambiguous

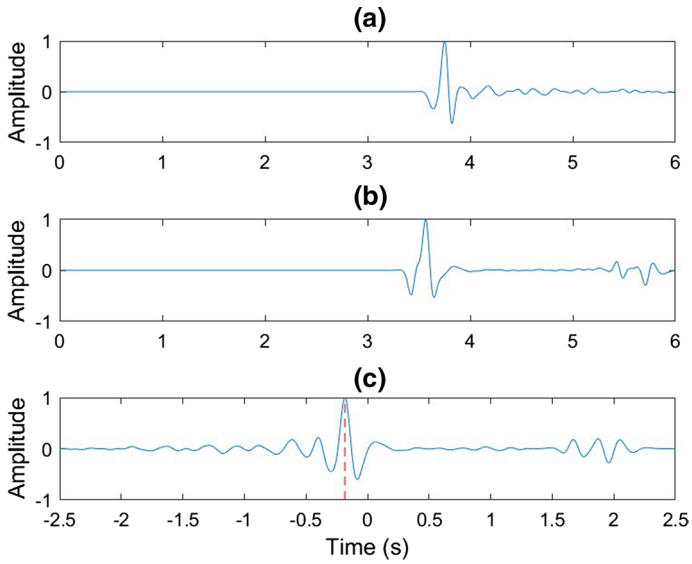


Fig. 1 A simple example of crosscorrelation between an observed trace (a) and a calculated trace (b). The maximum value of the resultant crosscorrelation trace (c) identifying the correct travel time difference (the red dash line) between these two traces

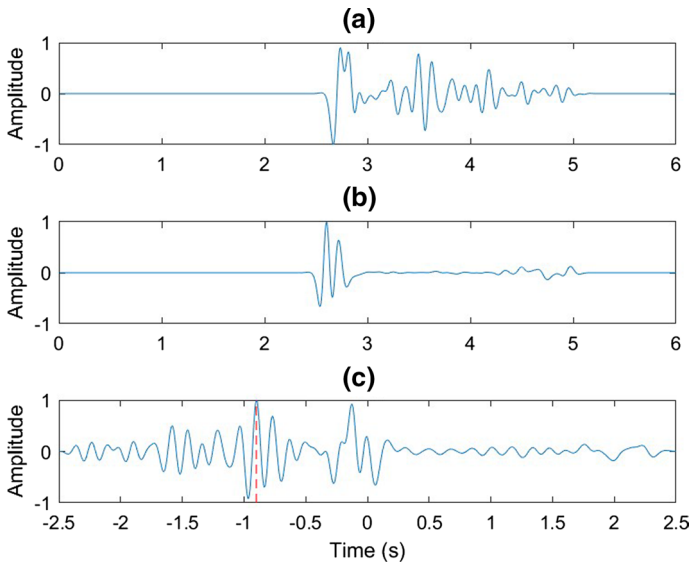


Fig. 2 A complicated example of crosscorrelation between an observed trace (a) and a calculated trace (b). Each trace contains multi-wave modes in addition to the desired transmitted waves. The maximum value of the crosscorrelation trace (c) provides the incorrect traveltme difference (the red dash line) between these two traces

results about the correct time lags (the red dash line). Specifically, the correct time-delay of the first arrivals between *A* and *B* may occur at the peak around time zero rather than the red dash line. To separate target components from unwanted noises and produce an improved SNR crosscorrelation, we compute the crosscorrelation in the wavelet domain to exploit the non-stationary variations of seismic traces.

3 Crosscorrelation Within the Wavelet Domain

It is well-known that the wavelet coefficient provides a local time and frequency distribution of the seismic traces. For a given seismic trace $X(t)$, the forward continuous wavelet transform is represented as:

$$\Psi_x^\varphi(f, \lambda) = \frac{1}{\sqrt{f}} \int_0^T X(t) \varphi_r\left(\frac{t-\lambda}{f}\right) dt, \tag{4}$$

where $\Psi_x^\varphi(f, \lambda)$ is a wavelet coefficient and φ_r denotes the complex Morlet wavelet. The symbols f and λ are the frequency (wavelet) and local time, respectively. This transform maps a 1D seismic trace to the 2D TF domain. Taking advantage of the capability to characterize non-stationary signals, we perform the crosscorrelation (Eq. (1)) in the wavelet domain to address frequency-dependent time-delays. The wavelet-domain crosscorrelation (Zhao and Li 2018b) is defined as:

$$WM(f, \tau) = \int_0^T \Psi_A^\varphi(f, \lambda) \Psi_B^\varphi(f, \lambda + \tau) d\lambda, \tag{5}$$

where $\Psi_A^{\varphi*}$ and Ψ_B^φ are the wavelet coefficients of noisy wavefields recorded at the receiver *A* and *B*, respectively. The wavelet crosscorrelation function $WM(f, \tau)$ is defined in such a way that it is not only a function of the time delay τ but also of the wavelet frequency f . It allows for the detection of non-stationary coherence structures and the potential travel time difference. $WM(f, \tau)$ is a complex-valued function, so the original phase of the recorded data is normally retained to honor the kinematics of travel time. This approach is a phase-preserving technique, and subsequent filtering is only applied to the amplitude spectrum.

We use the wavelet transform (Eq. (4)) in the complicated trace example (Fig. 2) and obtain the wavelet coefficients of the observed trace shown in Fig. 3. The wavelet crosscorrelation (Eq. (5)) expands the coefficients into the f, τ domain and helps to determine the delay between both traces at each frequency. It is better for characterizing different wave-modes than conventional crosscorrelation (Fig. 4a). Therefore, target detections in the 2D TF domain are required to extract the preferred wave-modes.

4 Single-Channel Estimation via Object Detection

The target wave-mode extraction in the wavelet TF domain is a classical problem of object detection in computer vision. Object detection refers to the ability of a computer to locate objects in an image and identify each object. This approach has been widely used for face and vehicle detection, as well as pedestrian counting, web images, security systems, and

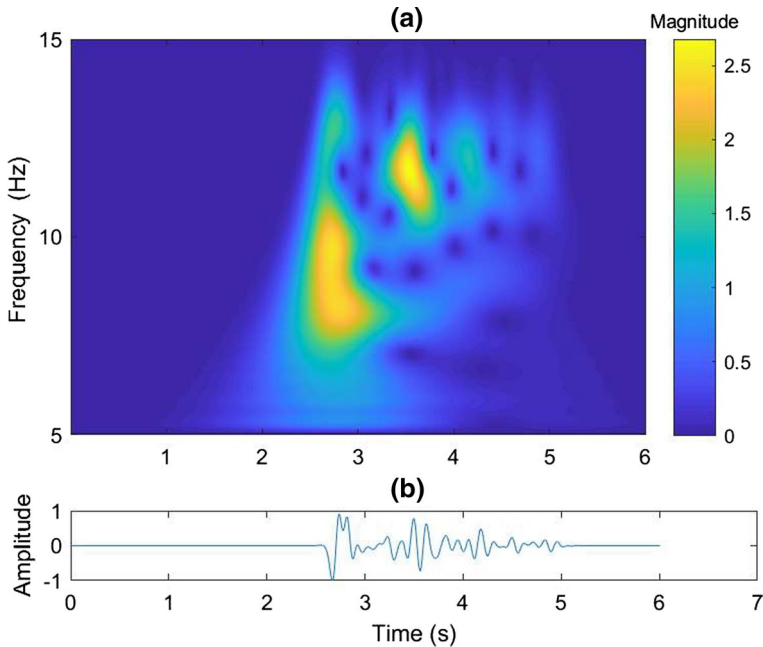


Fig. 3 The wavelet coefficients of the observed trace in the TF domain (a) and the corresponding time-domain trace (b)

driverless cars (Girshick et al. 2014). The first step of traditional object detection is image segmentation that partitions a digital image into multiple segments. This can be posed as a graph partitioning problem (or energy minimization problem), or formulated as a solution to a partial differential equation (Shi and Malik 2000). Thresholding is the simplest non-contextual segmentation technique. This study implements a locally adaptive-threshold algorithm for 2D TF images (Bradley and Roth 2007; Efford 2000). The adaptive threshold function chooses the soft threshold based on the local average magnitude of the wavelet coefficients in the neighborhood of each window. The values lower than the average magnitude within the filtered window, with a specified size, are set to zero. The windowed thresholding filter, denoted as $H(f, \tau)$, applied to the obtained wavelet crosscorrelation $WM(f, \tau)$ and is defined from Eq. (5) as:

$$\begin{aligned}
 WM_o(f, \tau) &= H(f, \tau) * WM(f, \tau) \\
 WM_T(f, \tau) &= \begin{cases} 0, & \text{for } WM(f, \tau) \leq \eta \cdot \max(WM_o(f, \tau)), \\ WM_o(f, \tau), & \text{for } WM(f, \tau) > \eta \cdot \max(WM_o(f, \tau)) \end{cases}, \quad (6)
 \end{aligned}$$

where $*$ denotes the 2D convolution operator and η the thresholding value. $WM_o(f, \tau)$ and $WM_T(f, \tau)$ are the output wavelet crosscorrelations after windowing and thresholding in the TF domain, respectively. $H(f, \tau)$ is designed with an adjusted length, for f and τ , to capture the event pattern. Here, we set up the parameters $f = 2$ Hz, $\tau = 1$ s, $\eta = 5\%$ for the sliding patch. A standard morphological (Vincent 1993) reconstruction is applied afterward to extract the connected components from $WM_T(f, \tau)$. Figure 4b illustrates the process of the locally adaptive thresholding and reconstruction from Fig. 4a, where it effectively isolates these wave objects from the background.

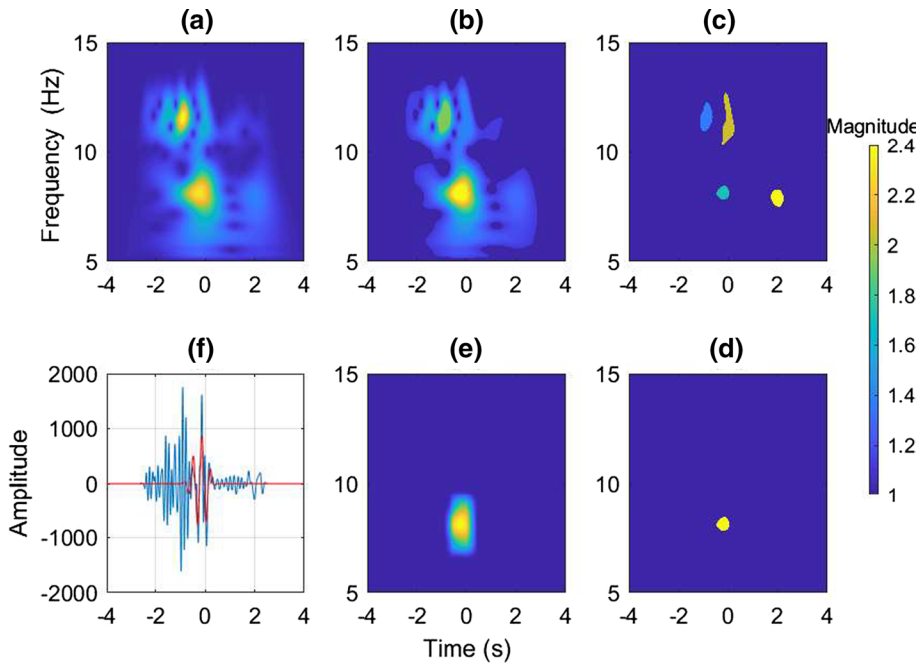


Fig. 4 A summary workflow of each detection step. The wavelet coefficients of the wavelet crosscorrelation (a) and the corresponding crosscorrelation trace (Fig. 2) in the time domain (f). Equation effectively isolates these wave objects from the background and after the locally adaptive thresholding (b). Label matrix of different wave-modes from the thresholded wavelet crosscorrelation coefficients (c), where different colors represent labels associated with different wave-mode-objects. The target wave-mode is selected and labeled by the yellow color (d). The corresponding wavelet coefficients (e) of the selected wave-mode from the label matrix. The inversed wavelet transform of the decomposed wave-mode is shown by the red line (f), in contrast with the original crosscorrelation trace with the blue line

Several wave objects are observed in Fig. 4b, but the resolution is still not enough to identify the target wave-modes from one another. We compute the regional maxima value to further improve the spatial resolution. Regional maxima are connected components of these wavelet crosscorrelation coefficients with a constant magnitude value, surrounded by zero values. The detailed algorithm can be found in Kong et al. (2010). We then obtain a label matrix of contiguous regions that contain labels for each wave-mode object recognized by its regional maxima (Haralick and Shapiro 1992). The zero values represent the background; the values labeled 1 construct the first wave-mode object; the values labeled 2 build a second wave-mode object, and so on. It mathematically formulates as

$$WM_R(f_{rmax}^j, \tau_{rmax}^j) = \text{region_max}\{WM_T(f, \tau) | \tau \in [-T, T], f \in [0, F]\}, \quad (7)$$

where WM_R denotes the output labels from WM_T (Eq. (6)). $f_{rmax}^j, \tau_{rmax}^j$ represents the regional maxima (rmax) values with frequency f and time τ for each object label j , respectively. The resulting label matrix consists of four wave-mode objects (Fig. 4c). From prior knowledge, we know that the correct τ associated with the first arrivals should be close to time zero and be presented in the low-frequency bandwidth. The light-green label (Fig. 4d) is then selected to be the target wave-mode ($WM_R(f_{rmax}^j, \tau_{rmax}^j) \rightarrow WM_R(f^{tar}, \tau^{tar})$) that

describes the correct travel time difference. The target region $WM_R(f^{tar}, \tau^{tar})$ of the wavelet crosscorrelation coefficients in the 2D TF Cartesian coordinate is recovered, as shown in Fig. 4e. The length len^{tar} and the width wid^{tar} associated with the target region $WM_R(f^{tar}, \tau^{tar})$ are stored. At last, the inverse wavelet transform brings the seismic trace back to the time domain. The inverse transform of this filtered wavelet coefficient $M_R(\tau^{tar})$ produces the red trace (Fig. 4f) with significantly better time-delay information compared with conventional crosscorrelation (the blue trace), shown as:

$$M_R(\tau^{tar}) = \frac{1}{C_{\varphi_r}} \int_0^F \int_0^T WM_R(f^{tar}, \tau^{tar}) \frac{1}{\sqrt{f}} \varphi_r\left(\frac{t-\tau}{f}\right) d\tau \frac{df}{f^2}, \quad (8)$$

where C_{φ_r} and F are the scaling factor of Morlet wavelet and effective bandwidth (Mallat and Zhang 1993), respectively.

Figure 4 summarizes a workflow of the traveltim difference estimation via object detection for the single-channel time-delay determination. It includes (a) the wavelet cross-correlation $WM(f, \tau)$, (b) local adaptive thresholding $WM_T(f, \tau)$, (c) label matrix estimation $WM_R(f_{rmax}^j, \tau_{rmax}^j)$, (d) the target region $WM_R(f^{tar}, \tau^{tar})$, and (e) the inverse wavelet transform $M_R(\tau^{tar})$. These five steps gradually decompose different correlated wave-modes in the 2D TF domain and result in a correct delay-time. This workflow only works for a single-channel case and often yields unsustainable results over different offsets. For application to field data, however, this may involve multi-dimensional time-delay determinations and a lack of prior knowledge for the target wave-mode. To tackle this problem, we add the space dimension to this proposed workflow and develop a multi-channel method. The stored information f^{tar} , τ^{tar} , wid^{tar} , len^{tar} (lower case) of the target region from each single-channel estimation combines to provide accurate multi-dimensional and sustainable travel time differences over offsets.

5 Multi-channel Estimation via Object Tracking

Similar to the single-channel estimation by object detection, the multi-channel estimation for the desired target wave-modes can be again treated as an object-tracking task in computer vision (Weng et al. 2006). It tracks the target wave-mode from correlated trace to trace to identify the position of the target label in consecutive offsets (Yussiff et al. 2014). The problem of multi-channel tracking is to instantaneously detect and predict the position and size of the target wave-mode over a sequence of offsets. The prediction is updated as the traces increase in offsets, based on the output of the target wave-mode detection of each offset. The goal is to use a series of wave-object detections over offsets, containing noise and other inaccuracies. This can produce a more accurate estimation of wave-mode tracking than those using single-channel detection alone (Hargrave 1989). The Kalman filter provides a mechanism to achieve this as it consists of three steps: (a) prediction: based on the knowledge of the target wave-mode and kinematic equations from the previous trace. This study predicts the position and size of the target wave-mode for the next trace; (b) detections: perform single-channel estimation and detect the target wave-mode and compare it with the prediction; (c) update: revise our estimation of the position and size of the target wave-mode by minimizing the covariance matrix between prediction and detections. The idea is to use previous offset to

predict the current offset and use the current measurement to correct the offset. This recursive iterative process of the prediction step consists of

$$\tilde{\mathbf{Y}}_{k+1} = \Phi \mathbf{Y}_k + \mathbf{N}_k, \quad \mathbf{N}_k \approx \text{normal}(0, \mathbf{Q}), \tag{9}$$

and predict the error covariance

$$\tilde{\mathbf{P}}_{k+1} = \Phi \mathbf{P}_k \Phi^T + \mathbf{Q}, \tag{10}$$

where k is the offset-sequence-index that normally varies from near to far offset. All the noises are independent and identically distributed with zero means. The variables Φ are the model matrix and are assumed to be constant. \mathbf{Y}_k is the predicted vector of offset k containing six components: the predicted geometry information F_k^{tar} , Γ_k^{tar} , WID_k^{tar} , LEN_k^{tar} (upper case) of the target region, and its moving velocities along with the frequency V_k^f and delay-time direction V_k^τ , respectively. We use \sim signs to denote the estimations of the prediction $\tilde{\mathbf{Y}}_{k+1}$, $\tilde{\mathbf{P}}_{k+1}$ based on existing measurements at the current offset k . Because the seismic time series is typically comprised of a variety of noises, \mathbf{N}_k denotes normal distribution (Gaussian noises) with mean 0 and variance \mathbf{Q} . \mathbf{N}_k therefore is a zero-mean, timewise-uncorrelated, unit-variance \mathbf{Q} sequence with a Gaussian probability distribution function. Note that the upper- and lowercases represent the predicted and measured components, respectively. Given $\tilde{F}_{k+1}^{tar} = F_k^{tar} + V_k^f \times dt$, $\tilde{\Gamma}_{k+1}^{tar} = \Gamma_k^{tar} + V_k^\tau \times dt$, we may rewrite Eq. (9) in a matrix form:

$$\begin{bmatrix} \tilde{F}_{k+1}^{tar} \\ \tilde{\Gamma}_{k+1}^{tar} \\ \tilde{WID}_{k+1}^{tar} \\ \tilde{LEN}_{k+1}^{tar} \\ \tilde{V}_{k+1}^f \\ \tilde{V}_{k+1}^\tau \end{bmatrix} = \begin{bmatrix} 1 & & dt & & & \\ & 1 & & dt & & \\ & & 1 & & & \\ & & & 1 & & \\ & & & & 1 & \\ & & & & & 1 \end{bmatrix} \begin{bmatrix} F_k^{tar} \\ \Gamma_k^{tar} \\ WID_k^{tar} \\ LEN_k^{tar} \\ V_k^f \\ V_k^\tau \end{bmatrix} + \begin{bmatrix} \exp(F_k^{tar}/2Q) \\ \exp(\Gamma_k^{tar}/2Q) \\ \exp(WID_k^{tar}/2Q) \\ \exp(LEN_k^{tar}/2Q) \\ \exp(V_k^f/2Q) \\ \exp(V_k^\tau/2Q) \end{bmatrix} \tag{11}$$

\mathbf{P}_k is the predicted error covariance matrix associated with \mathbf{Y}_k :

$$\mathbf{P}_k = \begin{bmatrix} \text{Cov}\{F_k^{tar}\} & & & & & & & \\ & \text{Cov}\{\Gamma_k^{tar}\} & & & & & & \\ & & \text{Cov}\{WID_k^{tar}\} & & & & & \\ & & & \text{Cov}\{LEN_k^{tar}\} & & & & \\ & & & & \text{Cov}\{V_k^f\} & & & \\ & & & & & \text{Cov}\{V_k^\tau\} & & \\ \text{Cov} = E\{(\mathbf{Y}_k - \mu(\tilde{\mathbf{Y}}))(\mathbf{Y}_k - \mu(\tilde{\mathbf{Y}}))^T\} & & & & & & & \end{bmatrix} \tag{12}$$

where E , μ stands for expected and mean value of the predicted vectors, respectively. The steps of measurements and updates consist of computing Kalman Gain

$$\mathbf{G} = \tilde{\mathbf{P}}_{k+1} \mathbf{H}^T [\mathbf{H} \tilde{\mathbf{P}}_{k+1} \mathbf{H}^T]^{-1}, \tag{13}$$

and update predictions with measurements

$$\mathbf{Y}_{k+1} = \tilde{\mathbf{Y}}_{k+1} + \mathbf{G} (\mathbf{Z}_{k+1} - \mathbf{H}\tilde{\mathbf{Y}}_{k+1}), \tag{14}$$

and update covariance error

$$\mathbf{P}_{k+1} = (\mathbf{I} - \mathbf{GH}) \tilde{\mathbf{P}}_{k+1}, \tag{15}$$

Similar to Φ , \mathbf{H} is the model matrix and is assumed to be constant

$$\mathbf{H} = \begin{bmatrix} 1 & & & \\ & 1 & & \\ & & 1 & \\ & & & 1 \end{bmatrix}, \tag{16}$$

where \mathbf{H} is formed as an identify matrix due to the simple mapping relationship from the measurements to the predictions. \mathbf{Z}_{k+1} is the measurement vector of offset $k + 1$ containing measured geometry information f_{k+1}^{tar} , τ_{k+1}^{tar} , wid_{k+1}^{tar} , len_{k+1}^{tar} (lowercases) associated with detected from the single-channel estimation (Fig. 4). In summary, these measured inputs \mathbf{Z} automatically update these predictions \mathbf{Y} , \mathbf{P} , \mathbf{G} for each offset, while Φ and \mathbf{H} remain as constant. The final output \mathbf{Y}_{k+1} can be expressed as a single equation without \sim sign.

$$\mathbf{Y}_{k+1} = (\Phi\mathbf{Y}_k + \mathbf{N}_k) + (\Phi\mathbf{P}_k\Phi^T + \mathbf{Q}) \mathbf{H}^T [\mathbf{H} (\Phi\mathbf{P}_k\Phi^T + \mathbf{Q})\mathbf{H}^T]^{-1} (\mathbf{Z}_{k+1} - \mathbf{H} (\Phi\mathbf{Y}_k + \mathbf{N}_k)), \tag{17}$$

and we use this equation for actual computation.

6 Examples

In this section, the proposed workflow is implemented in several examples, including active and passive sources from exploration and global seismology, respectively. We aim to demonstrate the robustness of this crosscorrelation function. The first example is the 2004 BP model from exploration seismology. We heavily smoothed the true velocity model as the initial model. The observed seismic records with a typical streamer acquisition are shown in Fig. 5a, and the calculated records generated by the smoothed velocity model are displayed in Fig. 5b. As indicated by the classical traveltimes tomography (Luo and Schuster 1991; Van Leeuwen and Mulder 2010), only transmitted seismic records (all other arrivals are windowed out) are used for crosscorrelation. The proposed workflow is then evaluated on the muted dataset, which contains traces from 50 to 87 km. The zero-offset detection via single-channel estimation serves as the initial values for the Kalman filter tracking system.

Similar to Fig. 4, Fig. 6 illustrates a near-offset example but with the proposed Kalman filtering workflow. The crosscorrelation gathers are created by the conventional crosscorrelation between the observed (Fig. 5a) and calculated gathers (Fig. 5b). The selected near-offset trace is marked with a vertical red dash line (Fig. 6a), and its wavelet crosscorrelation coefficients are displayed in Fig. 6b. The detection (the light green label) is plotted in Fig. 6c against the prediction (the red bounding box). The result validates the proposed method as the detected wave-mode aligns very well with the predicted bounding box. Finally, the resulting wave-mode derived from the predicted bounding box is shown as the final selection (Fig. 6d). Figures 7 and 8 illustrate a middle- and far-offset trace example, respectively. As expected, the Kalman-based prediction (bounding boxes) always presents a decent agreement with the measurements in the presence of multi-wave-modes.

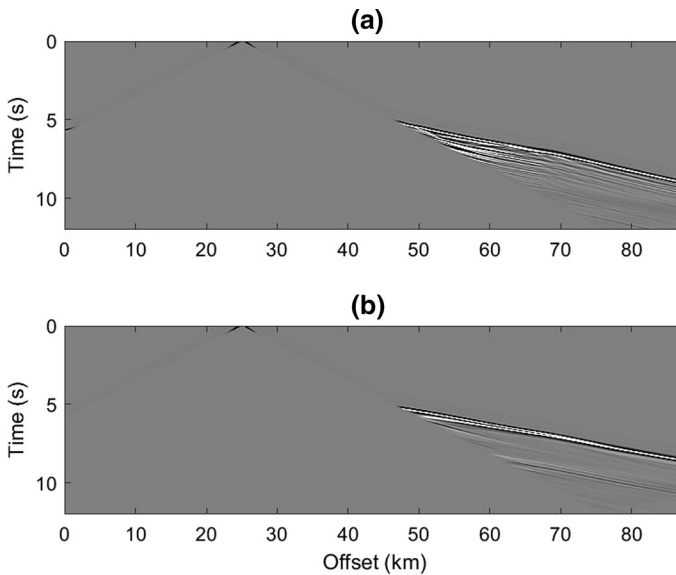


Fig. 5 Synthetic seismic records generated by BP 2004 exact velocity model **(a)** and initial smoothed **(b)** P-wave velocity models. Reflected and directed waves are muted for model building purposes

The observation supports the randomness and independence of the tracking errors, where the overall misfit error is always lower than 2%. The resulting comparisons of correlation gathers are illustrated in Fig. 9. The proposed predictions show good signal continuity on the resulting time-lags (the red lines) and show reduced contamination from other wave-modes. In contrast, the conventional crosscorrelation **(b)** appears much noisier with less continuity in terms of the resulting time-lag. These observations validate the robustness of the proposed workflow.

As the noise is a big part of any seismic data processing, we may exploit this synthetic example to examine the robustness of this workflow again at different noise levels. The Gaussian white noise of 50% variance (of maximum amplitude) is added to Fig. 4, and Fig. 10 demonstrates that the single-channel estimation is still valid. However, the presence of heavy Gaussian noises may bias the single-channel estimation over offsets. We may, therefore, take advantage of the noise terms $\mathbf{N}_k \approx \text{normal}(0, \mathbf{Q})$ of the multi-channel estimation in Eq. (17), since the Kalman updated-matrix equations yield minimum expected error and the optimum estimation, when the noise is assumed to be white, Gaussian, uncorrelated, and independent. Figures 11 and 12 show the Gaussian noises of 35%, and 65% variance (of maximum amplitude) is added to Fig. 9, respectively. Our multi-channel estimation, especially Fig. 12b, still delivers a high SNR crosscorrelation function despite the existence of substantial noises. Figure 13 summarizes the noise level tests and provides a quantitative assessment of these above figures.

The second example uses data from a downhole vertical well survey for monitoring hydraulic fractures in Sichuan province, China (Chen et al. 2018; Zuo et al. 2018). In this geometry, with receivers along a well (Fig. 14a), retrieving information from background noise is possible because the passive-source data (Fig. 14b) contain waves arriving from unknown natural sources to the receivers in 1.2 s. An example of interferometric crosscorrelation is presented in Fig. 15a, in which 10-day recordings of raw records are unable to

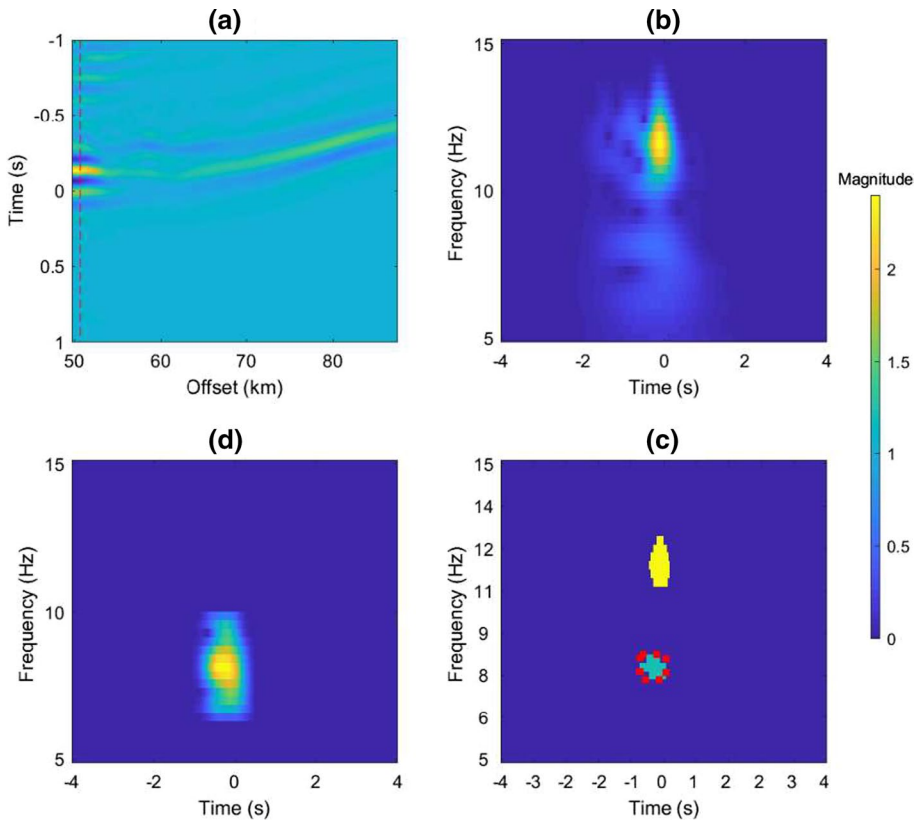


Fig. 6 A near-offset trace of the BP example including **a** the conventional crosscorrelation gather between the observed and calculated gathers; **b** the wavelet coefficients of the wavelet crosscorrelation; **c** the label matrix of two wave-modes from the thresholded wavelet crosscorrelation coefficients. The measured target wave-mode is colored as light green and the corresponding prediction by using the Kalman filter is marked as a red-dash bounding box; **d** the final selected wave-mode resulting from the Kalman prediction

produce results with good SNR (a zoom-in view can be founded in Fig. 17a). We treat the deepest receiver as a source and produced an anti-causal upgoing P-wave section by cross-correlating the vertical (along-the-well) receiver components. Noise sources generate the P-wave and are likely located above the receivers and likely relate to human activity on the well pad. Figure 15a shows the low SNR crosscorrelation gathers because natural sources are distributed nonuniformly in space and nonperiodic in time (Grechka and Zhao 2012; Zhao and Li 2018a). The spatial nonuniformity and the lack of temporal periodicity require the proposed workflow to enhance the reconstructed correlation gathers from background noise.

Similar to the previous BP example, Figs. 15, 16, and 17 illustrate three selected example traces with the proposed Kalman tracking and detection workflow. The autocorrelation (zero-offset) detection via single-channel estimation serves as the initial values for the Kalman filter tracking system. The autocorrelation trace is marked with a vertical red-dashed line (Fig. 15a), and its wavelet crosscorrelation coefficients are displayed in Fig. 15b. The detection (the light green label) is plotted in Fig. 15c against the prediction (the red bounding box). The results show that the proposed method as the detected

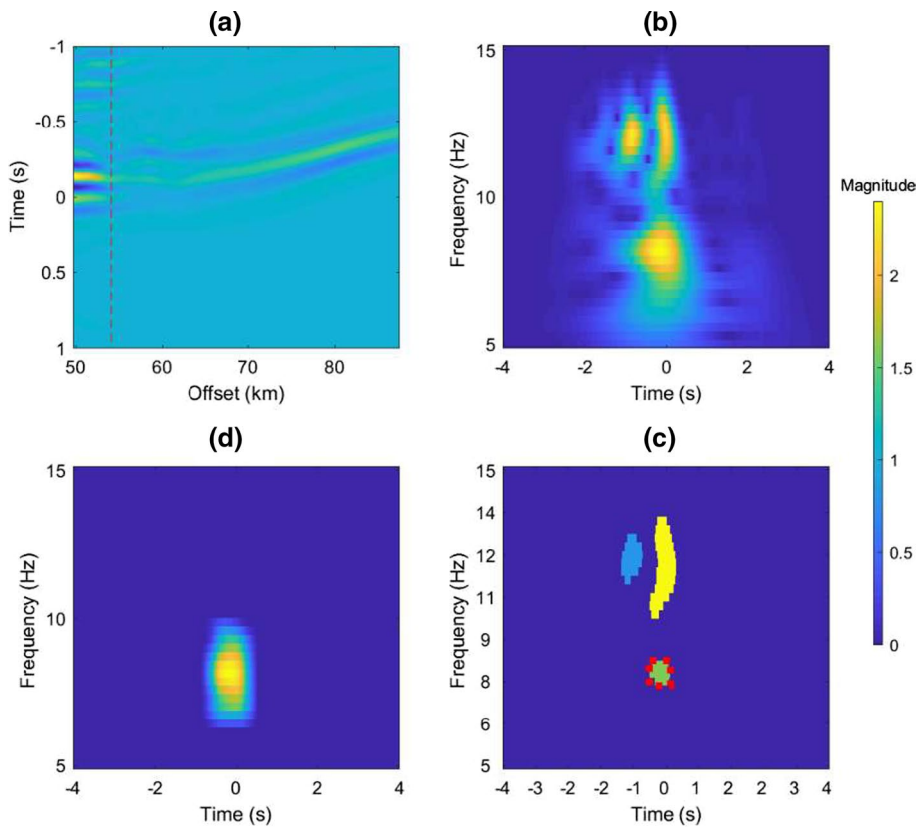


Fig. 7 A middle-offset trace of the BP example, displayed in the same fashion as Fig. 6

wave-mode aligns very well with the predicted bounding box. Finally, the resulting wave-mode derived from the predicted bounding box is shown as the final selection (Fig. 15d). Figure 16 illustrates another selected trace example. As expected, the Kalman-based prediction (bounding boxes) always presents a decent agreement with the measurements in the presence of multi-wave-modes. The observation supports the randomness and independence of the tracking errors, where the overall misfit error is always lower than 1%. The resultant comparisons of interferometric gathers are illustrated in Fig. 17. The proposed predictions show good signal continuity on the resulting peaks (the red lines in Fig. 17a) and demonstrate reduced contamination from other wave-modes.

The third example uses data from the vertical component of many broadband stations deployed around south Texas, shown in Fig. 18. The continuous signals were processed by removing the instrument response, mean value, and a linear trend, tapering the ends, decimating the records to 1 Hz, band-pass filtering between 0.02 and 0.2 Hz. We apply a time-domain-normalization to remove earthquake signals and instrumental irregularities and spectral whitening to enhance the ambient noise signal (Bensen et al. 2007). Finally, daily crosscorrelations were computed and stacked with a time-scale phase-weighted stack (Ventosa et al. 2017). The resultant crosscorrelation, shown in Fig. 19a, still experiences a low SNR issue due to insufficient ambient source coverage and robust stacking. In contrast,

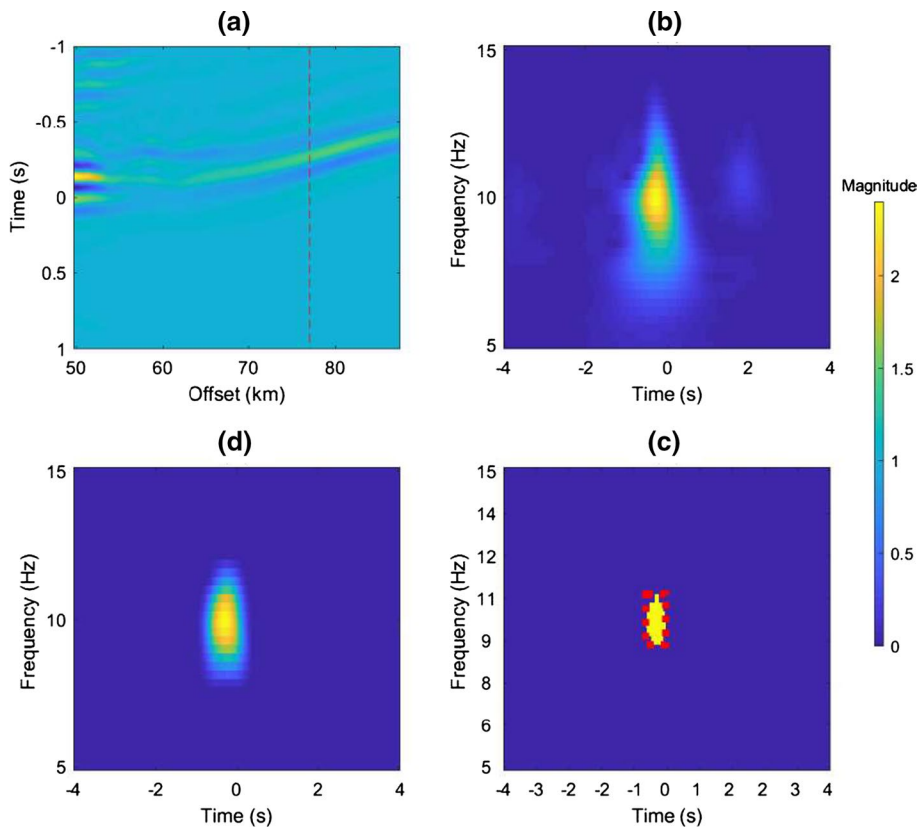


Fig. 8 A far-offset trace of the BP example, displayed in the same fashion as Fig. 6

our proposed method results in a high SNR for the target wave-mode (Fig. 19b). Given the similar nature presence of ambient noise, the Kalman tracking and detection steps display similar patterns to those of the second example (Figs. 15, 16, 17). Therefore, we bypass the illustrations of these steps to avoid showing repeated results from the previous examples.

7 Discussions

7.1 Wavelet-Domain Crosscorrelation and Waveform Detection

The single-channel stage is performed in the wavelet crosscorrelation domain, so it limits our capability to discriminate wave-modes in the presence of different frequencies and time. Wave-mode decompositions associated with other physical properties (wavenumber, angle) may perform in the corresponding domains (FK or radon domain) to achieve better detection and tracking. One notable drawback is the waveform segmentation and denoising during the single-channel estimation. We manually set up the thresholding parameters $\eta = 5\%$ of the maximum values of the target wave-mode. We are in a preliminary stage of implementation where the parameters are determined in a manual way instead of through

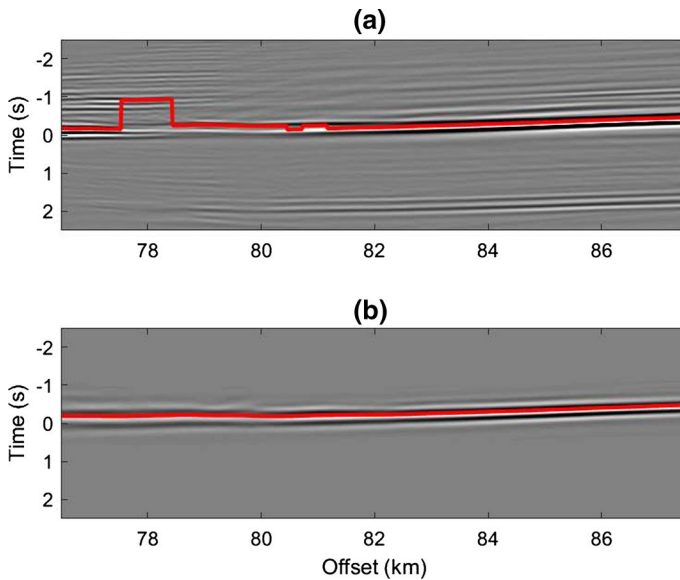


Fig. 9 The crosscorrelation gathers from the BP example, obtained from **a** conventional crosscorrelation and **b** wavelet crosscorrelation using the proposed wave-mode detections and Kalman predictions. The time delays picked by the maximum peak values are marked by the red lines. The wavelet crosscorrelation not only results in accurate time-lags but also yields a much higher SNR

automatically systematic optimization. Generally, small f and τ size with large η may overkill the target wave-mode, whereas large f and τ with small η do not remove background noise effectively. As discussed in the introduction section of microseismic denoising, the least-squares fitting for complex damping exponential components (Chen 2018) and fuzzy-/K-means clustering (Chen 2017)-based machine learning techniques are very promising to provide a fully automatic solution to this issue.

7.2 Kalman Filtering and Waveform Tracking

The prevalent benefit of multi-channel stages is tracking targets from near to far offsets since the near traces normally present better SNR comparing with far traces. Specifically, the zero offsets of seismic interferometry are the autocorrelation where the utmost SNR signal represents. It feeds as a high-quality initial input for the Kalman filter and helps the algorithm continuously track for a similar target in consecutive offsets. Having the noises terms \mathbf{N}_k in Eq. (17), the Kalman filter is very insensitive to these incoherent noises by minimizing the covariance matrix between prediction and measurements. Noisy examples (Figs. 11, 12) for Fig. 9 demonstrate the robustness as an automatic tracking system. On the other hand, the current multi-channel system assumes a constant Φ and H , and constraint us to track one wave-mode over offsets. The presence of multiple wave-modes or coherent noises often results in strong non-stationarity which requires dynamic Φ and H . To simultaneously track multiple wave-modes or remove coherent noises in the future, we may approximate non-stationarity by a series of local stationary components or develop non-stationary Φ and H over offsets (Chen 2018).

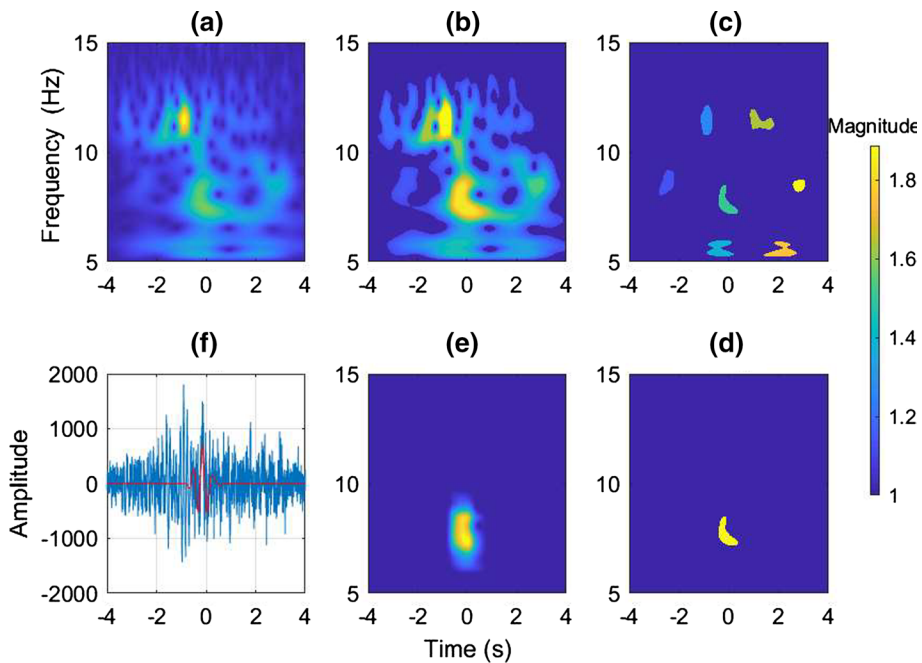


Fig. 10 Noise sensitivity test of the robustness of the single-channel estimation workflow shown in Fig. 4. A Gaussian noise with 50% (of maximum amplitude) variance is added to the original crosscorrelation (a). Our method effectively isolates these wave objects from the background and after the locally adaptive thresholding (b). Label matrix of different wave-modes from the thresholded wavelet crosscorrelation coefficients (c), where different colors represent labels associated with different wave-mode-objects. The target wave-mode is selected and labeled by the yellow color (d). The corresponding wavelet coefficients (e) of the selected wave-mode from the label matrix. The final recovered wave-mode, shown in the red line (f), is still able to recover a high SNR result, in contrast with the noisy crosscorrelation trace with the blue line

7.3 Acquisition Requirements

Although Eq. (17) ensures a consistent multi-channel prediction (geometry of the bounding box) against the single-channel measurement, the algorithm still requires a high spatial sampling rate and a strong spatial correlation. A dense sampling prevents a significant lateral variation of the TF pattern of the target wave-mode, whereas a coarse acquisition of seismic stations may suffer from aliasing and strong background noises. To compensate for the sparse acquisition geometry, an effective interpolation technique is critical to make this proposed workflow feasible in practice. We did not encounter these obstacles from these three applications, because these correlated wave-modes behave in similar TF patterns and thusly the acquisition restrictions are relaxed.

7.4 Machine Learning and Future

If we like to extend our workflow into general denoising applications in addition to cross-correlation-interferometric studies, more advanced and comprehensive strategies are demanded to handle low SNR data as well as multi-wave contaminations. While dynamic non-stationary Kalman filter is an alternative way to proceed, machine learning is more

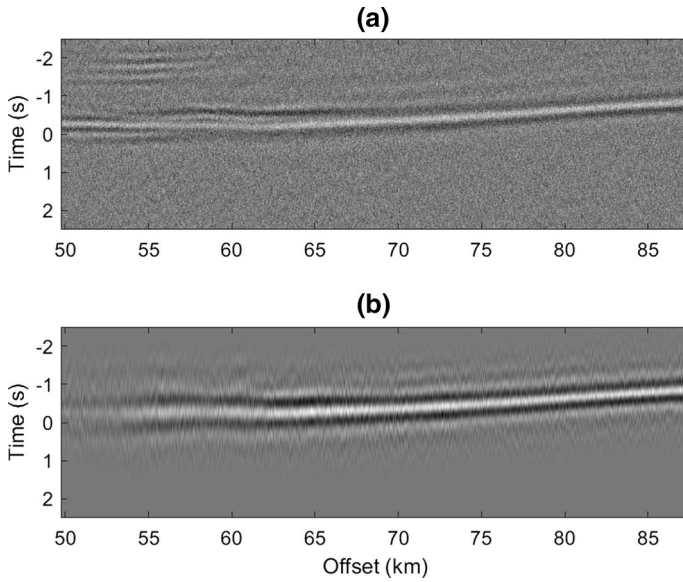


Fig. 11 Noise sensitivity test of the robustness of the multi-channel estimation workflow shown in Fig. 9. A Gaussian noise with 35% (of maximum amplitude) variance is added to the original crosscorrelation gather (a). The Kalman-filter incorporates these Gaussian noises into the error covariance of the predicted equation; therefore, our proposed methods still produce a higher SNR produce results (b)

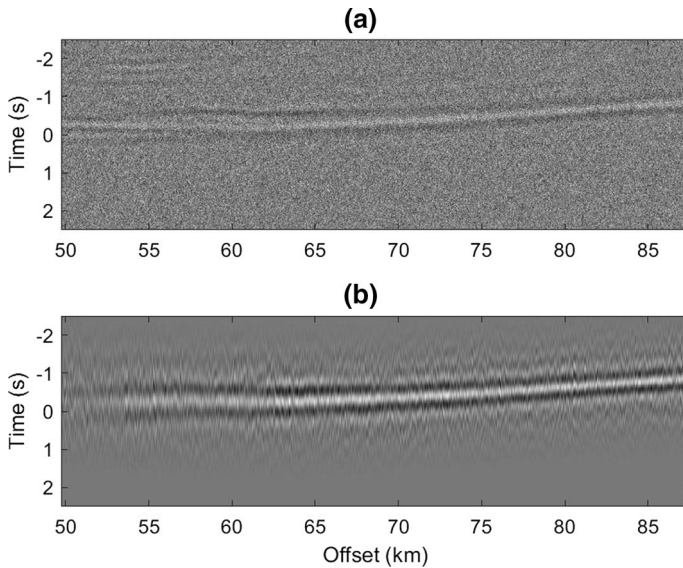


Fig. 12 Another noise sensitivity test of the robustness of the multi-channel estimation workflow shown in Fig. 9. A Gaussian noise with 65% (of maximum amplitude) variance is added to the original crosscorrelation gather (a) but still produces a higher SNR produce results (b)

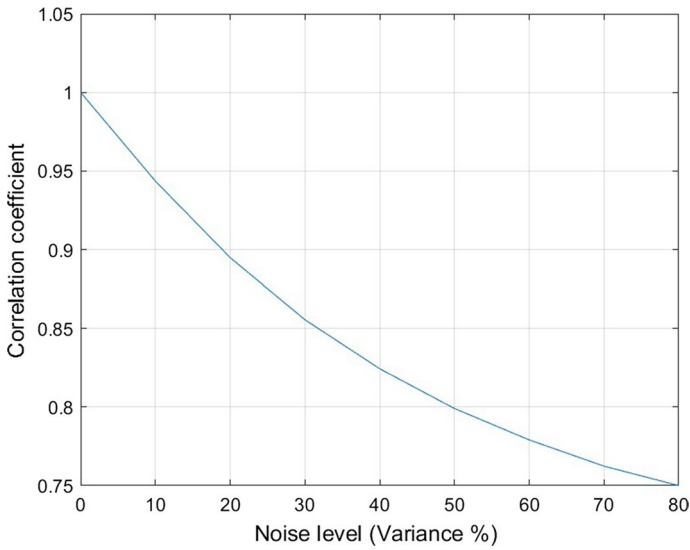


Fig. 13 Evaluation of Kalman filter-based multi-channel estimation with different noise levels. The performance is measured by correlation coefficients between Figs. 9, 11 and 12

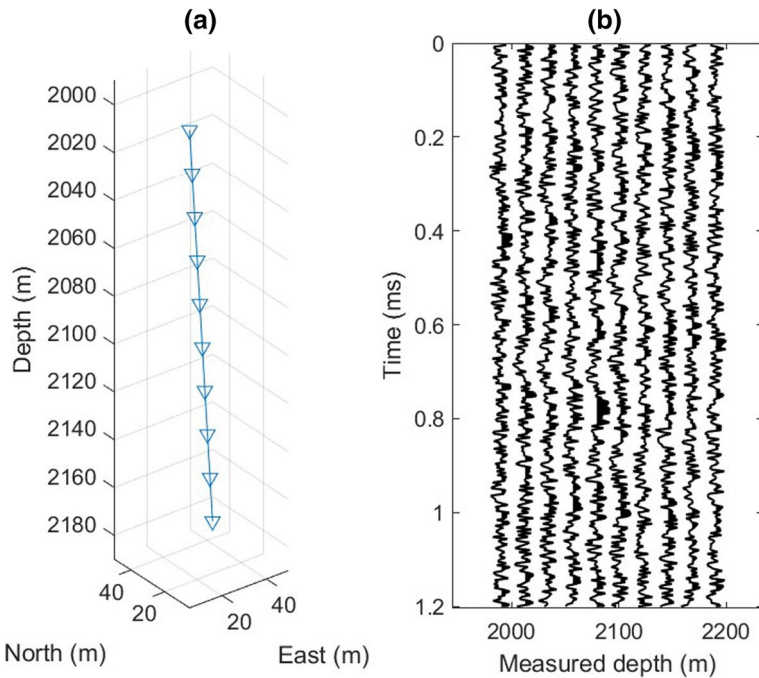


Fig. 14 **a** Well trajectory (blue) and locations of receivers (triangles) from the downhole example. The dip of the lateral section covered by the receivers is less than 2° , **b** randomly chosen 1.2-s-long microseismic background noise gather recorded by a string of 10 downhole receivers. This gather represents typical input data for the case studies discussed in this paper

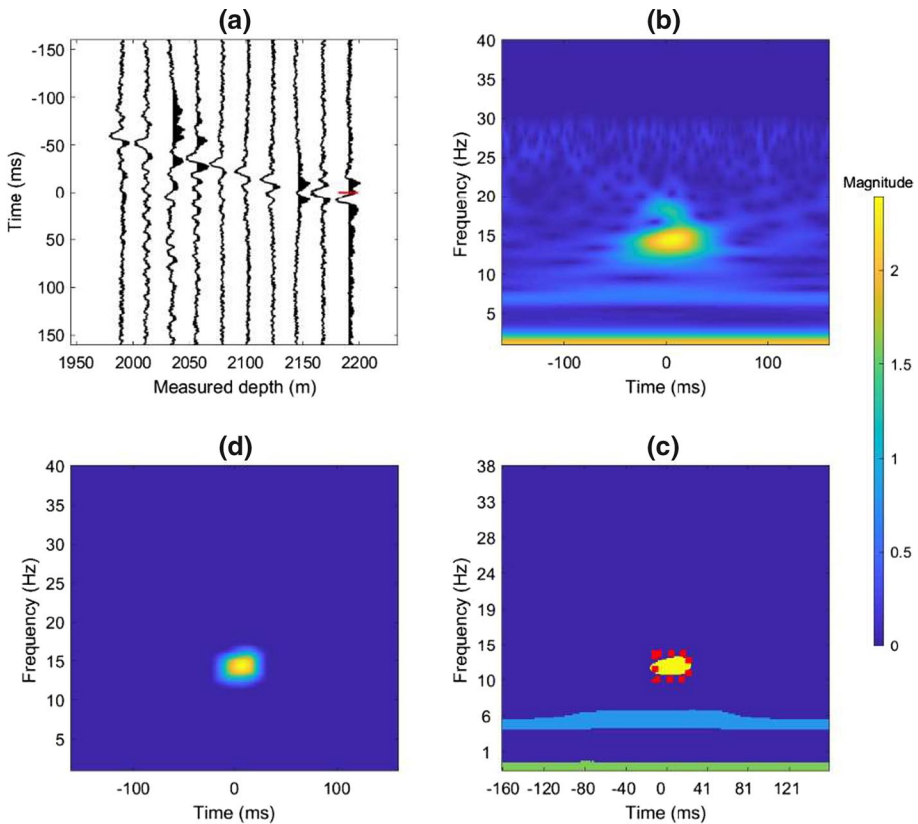


Fig. 15 A zero-offset trace, marked by a horizontal red line, from the downhole example, including **a** the interferometric crosscorrelation gather reconstructed from downhole receiver array using background noises (Fig. 14a); **b** the wavelet coefficients of the wavelet crosscorrelation; **c** the label matrix of three wave-modes from the thresholded wavelet crosscorrelation coefficients. The measured target wave-mode is colored yellow, and the corresponding prediction by Kalman filter is marked as a red-dashed bounding box; **d** the final selected wave-mode resulting from the Kalman prediction

attractive given its popularity nowadays. Based on our limited understanding, machine learning may be superior to conventional methods on four items: (1) the supervised machine learning relies on high-quality labels to train correct models. It is well-known that different denoising techniques are good at different noise scenarios. By combining trained labels from a variety of conventional methods, supervised machine learning may stand in a better position to tackle different noise types in one pass; (2) Modern seismic processing is moving toward to higher dimension (5D or 6D) and gradually becoming the standard industrial procedure. Many conventional techniques are still subjective to visualized-based human interventions, but machine learning easily surpassed the 3D limitation of human visualization and better separate signal and noises in a higher dimension; (3) Once adequate noise models are built, numerous labor costs are saved as machine learning reduces the human efforts. Noise models may be associated with certain acquisition geometry, geological features, and exploration purposes; (4) A few types of observed noises present extreme nonlinearity and non-stationarity beyond physics. Machine learning may serve as an addition to these physics-based methods. A comprehensive workflow consists

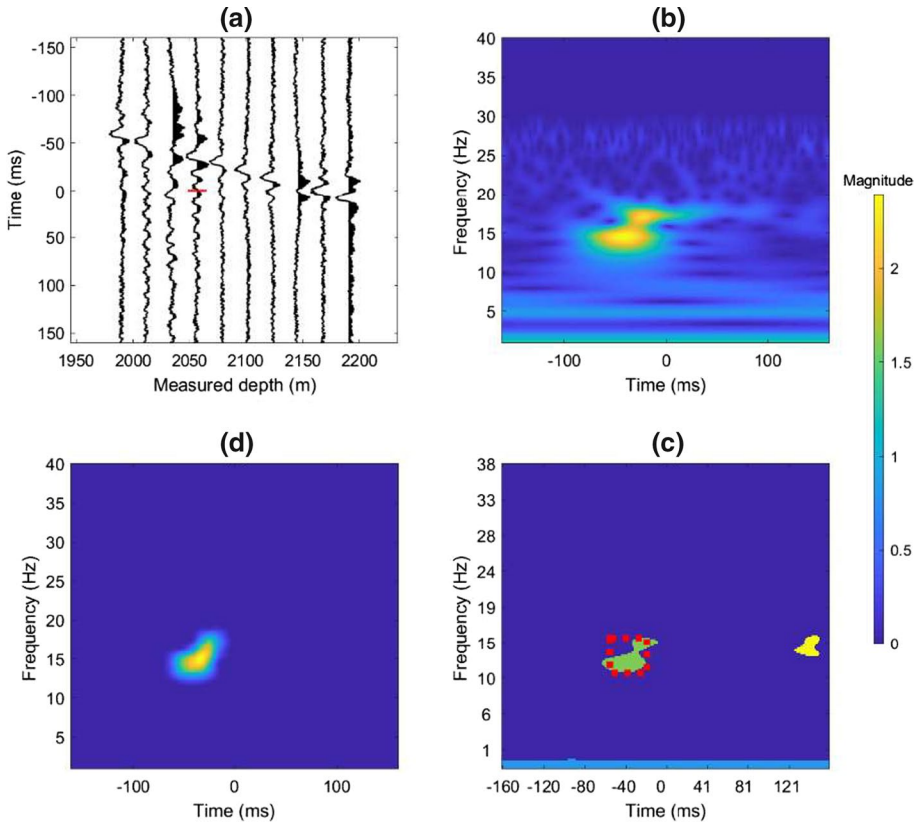


Fig. 16 A far-offset trace from the downhole example, marked by a horizontal red line, displayed in the same fashion as Fig. 15

of machine learning, conventional denoising algorithm, and manual involvement is the ongoing research directions.

8 Conclusions

We have developed a comprehensive technique to improve the quality of crosscorrelation functions in the wavelet domain. This method integrates wavelet transformation, crosscorrelation, image object detection, and Kalman-filter object tracking. This integration maintains the target wave-mode across frequencies and offsets and exploits object detection and tracking across different offset, which allows for better wave-mode separations. A robust target tracking and high-quality separation of multi-wave-modes are achieved using single- and multi-channels estimation of the wavelet-correlation coefficients. Conflicting issues of contaminations from other wave-modes are addressed. Results from three different applications demonstrate that this proposed technique can effectively isolate the target wave-modes and produce high SNR correlation gathers without requiring any further information. Within this framework, we have demonstrated the value of the proposed techniques

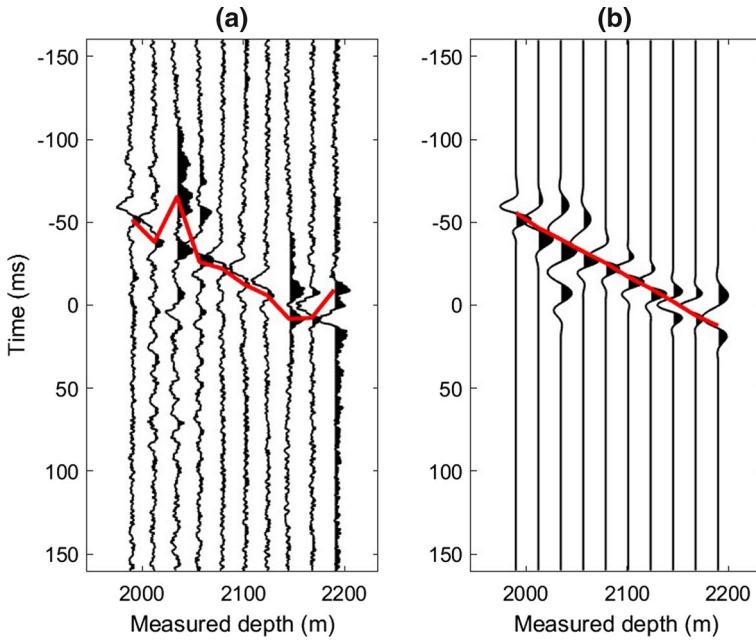


Fig. 17 Wave retrieved from **a** crosscorrelation that propagates in the direction from bottom to top in Fig. 14. The maximum value of each trace is connected by the red line resulting in an inconsistent slope. In contrast, the proposed methods deliver a high SNR gather, **b** the slope of the red line implies the average apparent velocity of 4.0 km/s

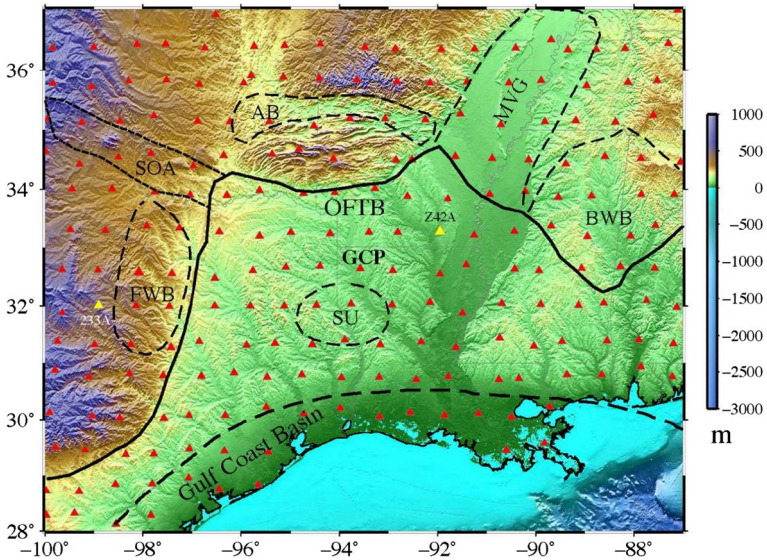


Fig. 18 Location of broadband seismological stations deployed around south Texas (inverted triangle) and the reference station Z42A is marked by yellow. The continuous data from these stations were used in the third example

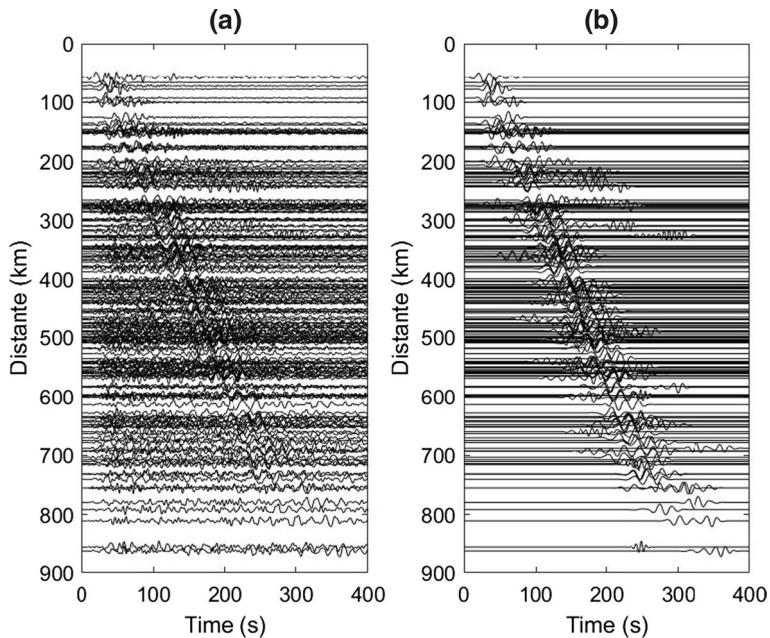


Fig. 19 Wave retrieved from **a** crosscorrelation that propagates directionally from south to north shown in Fig. 18. The proposed methods deliver a high SNR gather, **b** the slope of the arrivals times implies the average apparent velocity of 2.73 km/s

by reducing other wave-mode influences on the target signals and providing valuable cross-correlation inputs for a variety of applications in exploration and global seismology.

Acknowledgements We specifically express our appreciation to Cristina Young for her critical work on improving this paper. We would like to thank the Associate Editor, Prof. Jeffery Yu Gu, and one anonymous reviewer for their comments and suggestions, which significantly improved the quality of this paper. This study is jointly supported by the National Key R&D Program of China (2017YFC1500303), the Science Foundation of China University of Petroleum, Beijing (2462019YJRC007 and 2462020YXZZ047), and the Strategic Cooperation Technology Projects of CNPC and CUPB (ZX20190220). The associated data and codes used by this paper are available at the link with <https://github.com/zhaoayangprof/KalmanFilterCrosscorrelation.git>.

Author Contributions YZ conceived the presented idea, developed the theory and performed the computations. He wrote the initial version of the manuscript and verified the preliminary results. FN is in charge of two Grants, which are used to support this study. He also provided the data of broadband stations in Texas. ZZ organized these examples and delivered many insightful discussions in the early stage of this study. XL provided data platforms and computational resources. JC assisted in preparing the updated data and codes since the corresponding author was unable to access the resources which were associated with his previous employer. JY provided English language editing services and fixed grammar issues.

References

- Bensen GD et al (2007) Processing seismic ambient noise data to obtain reliable broad-band surface wave dispersion measurements. *Geophys J Int* 169:1239–1260
- Bishop G, Welch G (2001) An introduction to the Kalman filter. *Proc SIGGRAPH Course* 8:41

- Bradley D, Roth G (2007) Adaptive thresholding using the integral image. *J Graph Tools* 12:13–21
- Chen Y (2017) Automatic microseismic event picking via unsupervised machine learning. *Geophys J Int* 212:88–102. <https://doi.org/10.1093/gji/ggx420>
- Chen Y (2018) Non-stationary least-squares complex decomposition for microseismic noise attenuation. *Geophys J Int* 213:1572–1585. <https://doi.org/10.1093/gji/ggy079>
- Chen H, Niu F, Tang Y, Tao K (2018) Toward the origin of long-period long-duration seismic events during hydraulic fracturing treatment: a case study in the shale play of Sichuan Basin, China. *Seismol Res Lett* 89:1075–1083
- Crump ND (1974) A Kalman filter approach to the deconvolution of seismic signals. *Geophysics* 39:1–13
- Curtis A, Nicolson H, Halliday D, Trampert J, Baptie B (2009) Virtual seismometers in the subsurface of the Earth from seismic interferometry. *Nat Geosci* 2:700
- Diallo MS, Kulesh M, Holschneider M, Scherbaum F, Adler F (2006) Characterization of polarization attributes of seismic waves using continuous wavelet transforms. *Geophysics* 71:V67–V77
- Efford N (2000) Digital image processing: a practical introduction using java (with CD-ROM). Addison-Wesley Longman Publishing Co., Inc., Boston
- Emerick AA, Reynolds AC (2012) History matching time-lapse seismic data using the ensemble Kalman filter with multiple data assimilations. *Comput Geosci* 16:639–659
- Girshick R, Donahue J, Darrell T, Malik J (2014) Rich feature hierarchies for accurate object detection and semantic segmentation. In: Proceedings of the IEEE conference on computer vision and pattern recognition, pp 580–587
- Grechka V, Zhao Y (2012) Microseismic interferometry. *Lead Edge* 31:1478–1483
- Hafezi MM, Mirhosseini M (2015) Application of cross-correlation in pipe condition assessment and leak detection; using transient pressure and acoustic waves. *Resour Environ* 5:159–166
- Haralick RM, Shapiro LG (1992) Computer and robot vision, vol 1. Addison-Wesley, Reading
- Hargrave P (1989) A tutorial introduction to Kalman filtering. In: IEE colloquium on Kalman filters: introduction, applications and future developments. IET, pp 1/1–1/6
- Keane RD, Adrian RJ (1992) Theory of cross-correlation analysis of PIV images. *Appl Sci Res* 49:191–215
- Knapp C, Carter G (1976) The generalized correlation method for estimation of time delay. *IEEE Trans Acoust Speech Signal Process* 24:320–327
- Kong J et al (2010) Accelerating MATLAB image processing toolbox functions on GPUs. In: Proceedings of the 3rd workshop on general-purpose computation on graphics processing units. ACM, pp 75–85
- Labat D (2005) Recent advances in wavelet analyses: part 1. A review of concepts. *J Hydrol* 314:275–288
- Li H, Nozaki T (1997) Application of wavelet cross-correlation analysis to a plane turbulent jet. *JSME Int J Ser B Fluids Therm Eng* 40:58–66
- Li H, Wang R, Cao S, Chen Y, Huang W (2016) A method for low-frequency noise suppression based on mathematical morphology in microseismic monitoring. *Geophysics* 81:V159–V167. <https://doi.org/10.1190/geo2015-0222.1>
- Luo Y, Schuster GT (1991) Wave-equation traveltime inversion. *Geophysics* 56:645–653
- Mallat SG, Zhang Z (1993) Matching pursuits with time-frequency dictionaries. *IEEE Trans Signal Process* 41:3397–3415
- Mousavi SM, Langston CA, Horton SP (2016) Automatic microseismic denoising and onset detection using the synchrosqueezed continuous wavelet transform. *Geophysics* 81:V341–V355. <https://doi.org/10.1190/geo2015-0598.1>
- Nakata N, Snieder R, Tsuji T, Lerner K, Matsuoka T (2011) Shear wave imaging from traffic noise using seismic interferometry by cross-coherence. *Geophysics* 76:SA97–SA106
- Niu F, Silver PG, Daley TM, Cheng X, Majer EL (2008) Preseismic velocity changes observed from active source monitoring at the Parkfield SAFOD drill site. *Nature* 454:204
- Qu S, Guan Z, Verschuur E, Chen Y (2019) Automatic high-resolution microseismic event detection via supervised machine learning. *Geophys J Int* 218:2106–2121. <https://doi.org/10.1093/gji/ggz273>
- Saad OM, Chen Y (2020) Automatic waveform-based source-location imaging using deep learning extracted microseismic signals. *Geophysics*. <https://doi.org/10.1190/geo2020-0288.1>
- Shi J, Malik J (2000) Normalized cuts and image segmentation. *Departmental papers (CIS)*, p 107
- Silvia MT (1987) Chapter 11—Time delay estimation. In: Elliott DF (ed) *Handbook of digital signal processing*. Academic Press, San Diego, pp 789–855. <https://doi.org/10.1016/B978-0-08-05078-0-4.50016-3>
- Sun H-M, Jia R-S, Du Q-Q, Fu Y (2016) Cross-correlation analysis and time delay estimation of a homologous micro-seismic signal based on the Hilbert–Huang transform. *Comput Geosci* 91:98–104
- Van Der Hilst RD, De Hoop MV (2005) Banana-doughnut kernels and mantle tomography. *Geophys J Int* 163:956–961

- Van Leeuwen T, Mulder WA (2010) A correlation-based misfit criterion for wave-equation traveltime tomography. *Geophys J Int* 182:1383–1394
- Ventosa S, Schimmel M, Stutzmann E (2017) Extracting surface waves, hum and normal modes: time-scale phase-weighted stack and beyond. *Geophys J Int* 211:30–44
- Vincent L (1993) Morphological grayscale reconstruction in image analysis: applications and efficient algorithms. *IEEE Trans Image Process* 2:176–201
- Viola F, Walker WF (2003) A comparison of the performance of time-delay estimators in medical ultrasound. *IEEE Trans Ultrason Ferroelectr Freq Control* 50:392–401
- Weng S-K, Kuo C-M, Tu S-K (2006) Video object tracking using adaptive Kalman filter. *J Vis Commun Image Represent* 17:1190–1208
- Yilmaz Ö (2001) Seismic data analysis: processing, inversion, and interpretation of seismic data. Society of Exploration Geophysicists, Tulsa
- Yu Z, Ferguson J, McMechan G, Anno P (2007) Wavelet-radon domain dealiasing and interpolation of seismic data. *Geophysics* 72:V41–V49
- Yussiff A-L, Yong S-P, Baharudin BB (2014) Parallel Kalman filter-based multi-human tracking in surveillance video. In: 2014 international conference on computer and information sciences (ICCOINS). IEEE, pp 1–6
- Zhang G, Lin C, Chen Y (2020) Convolutional neural networks for microseismic waveform classification and arrival picking. *Geophysics* 85:WA227–WA240. <https://doi.org/10.1190/geo2019-0267.1>
- Zhao Y, Li W (2018a) Model-based radiation pattern correction for interferometric redatuming in 4D seismic. *Geophysics* 83:Q25–Q35
- Zhao Y, Li W (2018b) Wavelet-crosscorrelation-based interferometric redatuming in 4D seismic. *Geophysics* 83:Q37–Q47
- Zhao Y, Liu T, Tang G, Zhang H, Sengupta M (2019) Virtual-source imaging and repeatability for complex near surface. *Sci Rep* 9(1):1–8
- Zhao Y, Niu F, Liu H, Jia X, Yang J, Huo S (2020) Source-receiver interferometric redatuming using sparse buried receivers to address complex near-surface environments: a case study of seismic imaging quality and time-lapse repeatability. *J Geophys Res: Solid Earth*. <https://doi.org/10.1029/2020JB019496>
- Zuo Q, Tang Y, Niu F, Li G, Chen H, Tao K, Chen B (2018) Temporal variations of near-surface anisotropy induced by hydraulic fracturing at a shale play site in Southwest China. *J Geophys Res Solid Earth* 123:8032–8044

Publisher's Note Springer Nature remains neutral with regard to jurisdictional claims in published maps and institutional affiliations.

Affiliations

Yang Zhao¹  · Fenglin Niu² · Zhishuai Zhang³ · Xiang Li⁴ · Jinhong Chen⁵ · Jidong Yang⁶

¹ State Key Laboratory of Petroleum Resource and Prospecting, Unconventional Petroleum Research Institute, China University of Petroleum, 18 Fuxue Road, Changping District, Beijing 102249, China

² Department of Earth, Environmental and Planetary Sciences, Rice University, Houston, TX 77005, USA

³ Department of Geophysics, Stanford University, Stanford, CA 94305, USA

⁴ Broad Geophysical Technology, Houston, TX 77043, USA

⁵ Houston Research Center, Aramco Services Company, Houston, TX 77084, USA

⁶ University of Texas at Dallas, Dallas, TX 75080, USA